Quantum Dynamics Simulations Reveal Vibronic Effects on the Optical Properties of [n]Cycloparaphenylenes

V. Sivaranjana Reddy,*[†,‡] Cristopher Camacho,[‡,§] Jianlong Xia,[⊥] Ramesh Jasti,[⊥] and Stephan Irle*[†,‡]

[†]Institute of Transformative Bio-Molecules (WPI-ITbM), and [‡]Department of Chemistry Nagoya University, Furo-cho, Chikusa-ku, Nagoya 464-8602, Japan

[§]School of Chemistry, University of Costa Rica, San Pedro de Montes de Oca, San José 11501-2060, Costa Rica

[⊥]Department of Chemistry, Boston University, Boston, Massachusetts 02215, United States

S *Supporting Information*

ABSTRACT: The size-dependent ultraviolet/visible photophysical property trends of [n]cycloparaphenylenes ([n]CPPs, n = 6, 8, and 10) are theoretically investigated using quantum dynamics simulations. For geometry optimizations on the ground- and excited-state Born−Oppenheimer potential energy surfaces (PESs), we employ density functional theory (DFT) and time-dependent DFT calculations. Harmonic normal-mode analyses are carried out for the electronic ground state at Franck−Condon geometries. A diabatic Hamiltonian, comprising four low-lying singlet excited electronic states and 26 vibrational degrees of freedom of CPP, is constructed within the linear vibronic coupling (VC) model to elucidate the absorption spectral features in the range of 300−500 nm. Quantum nuclear dynamics is simulated within the multiconfiguration time-dependent Hartree approach to calculate the vibronic structure of the excited electronic states. The symmetry-forbidden $S_0 \rightarrow S_1$ transition appears in the longer wavelength region of the spectrum with weak intensity due to VC. It is found that the Jahn−Teller and pseudo-Jahn−Teller effects in the doubly degenerate S_2 and S_3 electronic states are essential in the quantitative interpretation of the experimental observation of a broad absorption peak around 340 nm. The vibronic mixing of the S_1 state with higher electronic states is responsible for the efficient photoluminescence from the S_1 state. The fluorescence properties are characterized on the basis of the stationary points of the excited-state PESs. The findings reveal that vibronic effects become important in determining the photophysical properties of CPPs with increased ring size.
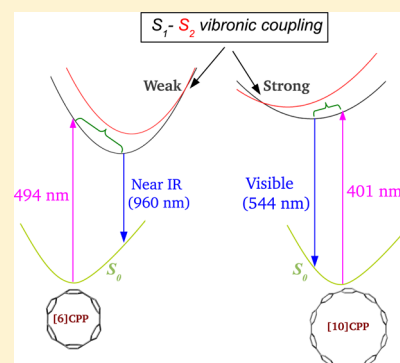
1. INTRODUCTION

[n]Cycloparaphenylenes ([n]CPPs, Figure 1) have been recently synthesized by several experimental groups, and the subsequent ultraviolet/visible (UV/vis) spectroscopic measurements revealed interesting and counterintuitive optical properties.[1−20] The photoexcited [n]CPPs exhibit an intense broad absorption peak with $\lambda_{max} \approx 338−340$ nm regardless of the ring size. In addition, a weak shoulder-like peak in the longer wavelength region of the absorption spectrum is also observed, particularly for the smaller CPPs. Interestingly, the maxima of the weak peak are blue-shifted with increasing ring size. The fluorescence measurements also reveal a blue-shift phenomenon of the emission maxima. The smallest known members of the CPP family, [5]- and [6]CPP, do not show any detectable visible fluorescence.[4,7,20] A large Stokes-shifted fluorescence is observed in the smaller CPPs; however, the extent of the shift decreases with increase of ring size.[1,8,12,17,19] The larger CPPs (above [14]CPP) emit at a relatively constant wavelength (~416 nm). A strong dependence of the quantum yields and fluorescence lifetimes on the ring size has also been reported. For example, the quantum yields of [8]- and [12]CPP are 0.08 and 0.66, respectively, and the corresponding lifetimes are 17.6 and 2.7 ns.[19] The single-exponential fluorescence decay seen in the experiments clearly demonstrates the absence of photoinduced
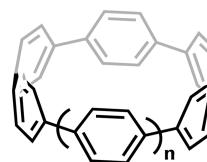
Figure 1. Schematic structure of [n]CPP, where n is the number of phenylene units.

intra- and intermolecular charge-transfer processes and emphasizes that the observed emission properties, indeed, are intrinsic to the CPPs.

Several theoretical studies attempted to uncover the experimental spectroscopic findings, predominantly examining the symmetries and relative energies of the frontier orbitals.[12,17,19,21−25] The key features in the experimental absorption and emission spectra were assigned on the basis of the calculated transition energies and oscillator strengths. The estimated large structural changes in the first excited state (S_1) accounted for the

experimentally observed Stokes shift in the smaller CPPs.[19] However, the $S_1 \rightarrow S_0$ transition is symmetry-forbidden and therefore cannot explain the observed bright emission. Possible symmetry-breaking effects via electron−hole interactions in the excited states were suggested by Wong on the basis of an analysis of evaluated transition density matrices and exciton binding energies.[21] In our previous work, we simulated the blue-shift and the double-peak profile in the emission spectra by performing direct quantum chemical molecular dynamics (MD) simulations on the excited-state Born−Oppenheimer potential energy surfaces (PESs) and found that larger CPPs emit from the S_2 and S_3 states, whereas smaller CPPs emit from the S_1 state.[26] However, it is apparent that the low-lying excited states, particularly in larger CPPs, are energetically very close and therefore require a non-adiabatic treatment in quantum chemical studies. For this reason, a thorough understanding of the ring-size-dependent optical properties on a rigorous quantum mechanical basis and detailed knowledge of the underlying photophysical mechanisms are still lacking.

The global minimum of even-membered CPPs in their ground state (S_0) is a fully alternant conformation of the p-phenylene units. The molecular point groups and the symmetries of the relevant excited electronic states are shown in Figure 2. Based on

Figure 2. Molecular point group of $[n]$CPPs (n = 6, 8, and 10) at the ground electronic state equilibrium geometry. Symmetries of the relevant electronic states are designated by the irreducible representation (IRREP) of the respective molecular point group.

elementary symmetry selection rules, the $S_0 \rightarrow S_1$ and $S_0 \rightarrow S_4$ transitions in CPP are dipole-forbidden. However, the $S_0 \rightarrow S_1$ transition is seen with very weak intensity in the electronic absorption spectrum of CPP.[4,7,8,12−17,19,20] Both the S_2 and S_3 states are doubly degenerate and possess the same irreducible representation (IRREP) of the molecular point group. The transitions from S_0 to these degenerate states are symmetry-allowed and are thus expected to contribute to the intense broad peak observed in the absorption spectrum at ~340 nm. Moreover, the S_2 and S_3 states are susceptible to a first-order Jahn−Teller (JT) distortion by doubly degenerate vibrational modes of appropriate symmetry. The JT-split components of the degenerate electronic states can interact with nearby electronic states. Such an interaction is known as a pseudo-Jahn−Teller (PJT) effect. The JT and PJT effects in the excited states of CPP are likely to be important in the interpretation of the underlying vibronic structure of the absorption spectrum and also for understanding the origin of the bright emission of large CPPs.

In the present study we investigate the photophysics of the low-lying excited states of $[6]$-, $[8]$-, and $[10]$CPPs by both electronic structure calculations and quantum nuclear dynamics. To this end, the vibronic interactions in the $S_1−S_2−S_3−S_4$

electronic manifold of CPP are studied within the well-established vibronic coupling (VC) model.[27] Time-dependent wave packet (WP) dynamics calculations are then employed to simulate the vibronic spectra of CPPs, and the obtained results are compared with the experiment. On the basis of these findings, the unusual CPP emission properties are discussed.

The rest of the paper is organized as follows. In section 2 we present the vibronic Hamiltonian. The details of the electronic structure calculations and the quantum nuclear dynamics are provided in section 3. Section 4 is concerned with results and discussion, and section 5 summarizes our results and concludes.

2. VIBRONIC HAMILTONIAN

As stated above, only the four low-lying excited electronic states are taken into account for each CPP to reproduce the observed experimental absorption spectral features in the range of 300−500 nm. From Figure 2, it is evident that these CPPs possess similar electronic configuration. The S_2 and S_3 states belong to the identical doubly degenerate IRREP of the respective symmetry point group. For $[6]$CPP, the symmetrized direct product of two E_u representations in the D_{3d} point group yields

$$(E_u)^2 = A_{1g} + E_g \qquad (1)$$

Similarly, the symmetrized direct products of two E_1 representations in the D_{4d} and two E_{1u} representations in the D_{5d} point groups yield

$$(E_1)^2 = A_1 + E_2 \qquad (2)$$

and

$$(E_{1u})^2 = A_{1g} + E_{2g} \qquad (3)$$

respectively. Based on the above elementary symmetry selection rules (eqs 1−3), both the S_2 and S_3 states of $[6]$CPP with E_u IRREP would undergo first-order JT splitting upon distortion along a degenerate vibrational mode of e_g symmetry. Likewise, the E_1 state(s) of $[8]$CPP would be split by e_2 vibrational modes, and the e_{2g} vibrational modes would lift the degeneracy of the E_{1u} state(s) of $[10]$CPP, as discussed in ref 26.

The other relevant linear intrastate and interstate coupling modes in the subset of electronic states are derived from the ansatz

$$\Gamma_m \otimes \Gamma_Q \otimes \Gamma_n \supset \Gamma_A \qquad (4)$$

Here, Γ_Q represents the IRREP of the symmetry point group of the molecule associated with the normal-mode Q. Γ_m and Γ_n denote the IRREPs of the electronic states m and n, respectively. Γ_A is the totally symmetric representation of the point group. Note that the totally symmetric vibrational modes are always active within the given electronic state. The vibrational modes of e_u symmetry act as coupling modes between the $S_1−S_2$ (and also $S_1−S_3$) states of $[6]$CPP. In a straightforward application of the above ansatz within the D_{4d} and D_{5d} point groups, it is found that the $S_1−S_2(S_3)$ electronic states of $[8]$- and $[10]$CPPs may interact via the e_1 and e_{1u} symmetry vibrational modes, respectively. For brevity, we assign the vibrational normal modes of CPP (Q_i) to three classes based on the coupling mechanism: totally symmetric (Q_t), JT active (Q_j), and PJT (Q_p) modes.

With the above description, the model Hamiltonian for treatment of the vibronic dynamics on the interacting $S_1−S_2−S_3−S_4$ electronic manifold of the CPPs in the diabatic electronic basis can be written as[27,28]

$$\mathcal{H} = (\mathcal{T}_N + \mathcal{V}_0)\mathbf{1}_6 +$$

$$
\begin{pmatrix}
E_{S_1}^0 + \boldsymbol{\kappa}^{(S_1)}\mathbf{Q}_t & \sum_p \lambda_p^{\prime(S_1,S_2)}Q_{px} & \sum_p \lambda_p^{\prime(S_1,S_2)}Q_{py} & \sum_p \lambda_p^{\prime(S_1,S_3)}Q_{px} & \sum_p \lambda_p^{\prime(S_1,S_3)}Q_{py} & 0 \\
 & E_{S_2}^0 + \boldsymbol{\kappa}^{(S_{2x})}\mathbf{Q}_t & \lambda^{(S_{2y})}\mathbf{Q}_{jy} & 0 & 0 & 0 \\
 & \quad + \lambda^{(S_{2x})}\mathbf{Q}_{jx} & & & & \\
 & & E_{S_2}^0 + \boldsymbol{\kappa}^{(S_{2y})}\mathbf{Q}_t & 0 & 0 & 0 \\
 & & \quad - \lambda^{(S_{2y})}\mathbf{Q}_{jx} & & & \\
 & h.\,c. & & E_{S_3}^0 + \boldsymbol{\kappa}^{(S_{3x})}\mathbf{Q}_t & \lambda^{(S_{3y})}\mathbf{Q}_{jy} & 0 \\
 & & & \quad + \lambda^{(S_{3x})}\mathbf{Q}_{jx} & & \\
 & & & & E_{S_3}^0 + \boldsymbol{\kappa}^{(S_{3y})}\mathbf{Q}_t & 0 \\
 & & & & \quad - \lambda^{(S_{3y})}\mathbf{Q}_{jx} & \\
 & & & & & E_{S_4}^0 + \boldsymbol{\kappa}^{(S_4)}\mathbf{Q}_t
\end{pmatrix}
\tag{5}
$$

where

$$\boldsymbol{\kappa}^{(S_\alpha)}\mathbf{Q}_t = \sum_t \boldsymbol{\kappa}_t^{(S_\alpha)}Q_t \quad \text{and} \quad \lambda^{(S_\alpha)}\mathbf{Q}_j = \sum_j \lambda_j^{(S_\alpha)}Q_j \tag{6}$$

Here, $E_{S_\alpha}^0$ represents the vertical excitation energy of the electronic state S_α (where $\alpha = 1, 2, 3,$ or 4) at the equilibrium geometry of the CPP. x and y represent the two components of the degenerate electronic state and the degenerate vibrational mode. The quantity κ_t is the intrastate linear coupling parameter for the totally symmetric vibrational mode t. The λ_j parameters denote the JT coupling of the JT-active mode j. The interstate linear coupling parameter, λ_p', is associated with PJT coupling mode p.

The quantity $(\mathcal{T}_N + \mathcal{V}_0)$ in eq 5 represents the Hamiltonian matrix associated with the ground electronic state of CPP and is defined in terms of dimensionless normal coordinates (Q_i) of unperturbed harmonic oscillators of frequency ω_i. In these coordinates the nuclear kinetic energy operator ($\mathcal{T}_N$) and the harmonic potential ($\mathcal{V}_0$) are expressed as

$$\mathcal{T}_N = -\frac{1}{2}\sum_t \omega_t\left(\frac{\partial^2}{\partial Q_t^2}\right) - \frac{1}{2}\sum_j \omega_j\left[\frac{\partial^2}{\partial Q_{jx}^2} + \frac{\partial^2}{\partial Q_{jy}^2}\right]$$
$$- \frac{1}{2}\sum_p \omega_p\left[\frac{\partial^2}{\partial Q_{px}^2} + \frac{\partial^2}{\partial Q_{py}^2}\right] \tag{7}$$

and

$$\mathcal{V}_0 = \frac{1}{2}\sum_t \omega_t Q_t^2 + \frac{1}{2}\sum_j \omega_j(Q_{jx}^2 + Q_{jy}^2)$$
$$+ \frac{1}{2}\sum_p \omega_p(Q_{px}^2 + Q_{py}^2) \tag{8}$$

The quantities ω_t, ω_j, and ω_p denote the harmonic frequency of the totally symmetric, JT, and PJT vibrational modes with the corresponding Q_t, Q_j, and Q_p coordinates of the ground state of the CPP, respectively. $\mathbf{1}_6$ in eq 5 represents a 6×6 unit matrix.

We need to emphasize here that, due to the larger dimensionality of the vibrational degrees of freedom entering into the Hamiltonian (eq 5), only the S_1–S_2 and S_1–S_3 PJT interactions of CPP are taken into account in the present investigation. These interactions seem to be adequate to interpret the major absorption and emission features of CPPs. The possible S_1–S_4, S_2–S_3, S_2–S_4, and S_3–S_4 interactions are important, particularly in the higher energy range of the absorption spectrum; however, they are neglected here for the sake of simplicity.

3. ELECTRONIC STRUCTURE CALCULATIONS AND QUANTUM NUCLEAR DYNAMICS SIMULATION

3.1. Computational Details. The electronic ground-state molecular structure of CPPs is optimized by utilizing density functional theory (DFT) with Becke's three-parameter functional in combination with the Lee–Yang–Parr correlation functional (B3LYP) and 6-311G(d) basis set. The harmonic vibrational frequencies (ω_i) are obtained by diagonalizing the force constant matrix of the optimized geometry of the electronic ground state. In addition to the vibrational frequencies, the transformation matrix from symmetry coordinates to mass-weighted normal coordinates is also obtained. Multiplying the latter coordinates by $(\omega_i)^{1/2}$ (in atomic units), we obtain the dimensionless normal displacement coordinates (Q_i).[29] The vertical excitation energies (VEEs) of CPP along each relevant vibrational mode for various nuclear geometries, $Q_i = \pm 0.25$ and ± 0.50 $(0.25) \pm 1.50$, are computed within the time-dependent (TD) DFT approach at the B3LYP/6-311G(d) level of theory. The computed energies plus the harmonic potentials of the electronic ground state of CPP are equated with the adiabatic potential energies (V) of the αth excited electronic state of CPP as a function of the dimensionless normal-mode displacement coordinates. A least-squares fitting procedure is utilized to evaluate the coupling parameters of the totally symmetric and JT vibrational modes.

The PJT coupling parameters (λ_p') can be obtained from

$$\lambda_p' = \frac{1}{2} Q_p^{-1} \times$$

$$[[V_2(Q_p) - V_1(Q_p)]^2 - [V_2(Q_0) - V_1(Q_0)]^2]^{1/2} \tag{9}$$

where V_1 and V_2 are the adiabatic potentials for the interacting electronic states. Q_0 represents the reference equilibrium configuration, and Q_p is the displacement from this reference configuration along the pth vibrational mode.

For comparison, the VEEs have also been computed by employing Coulomb-attenuating method B3LYP (CAM-B3LYP) and long-rang-corrected Perdew−Burke−Ernzerhof (LC-ωPBE) functionals in addition to B3LYP. These functionals predict excitation energies that are significantly blue-shifted with respect to experimental values, and therefore we will mostly limit our discussion to TD-B3LYP values that agree much better with experiment.

To explore the origin of the fluorescence properties, we have performed excited-state optimization calculations. The ground-state (S_0) and excited-electronic-state (S_1) geometries are optimized at the TD-B3LYP/6-31G(d) level of theory.

3.2. Quantum Nuclear Dynamics Simulations. The electronic absorption spectrum of CPP is calculated using the well-known Fermi's golden rule formula. The spectral intensity distribution, $P(E)$, is given by

$$P(E) = \sum_v |\langle \Psi_v^f | \hat{T} | \Psi_0^i \rangle|^2 \delta(E - E_v^f + E_0^i) \tag{10}$$

Here, $|\Psi_0^i\rangle$ represents the wave function of the vibronic ground state (with energy E_0^i), and $|\Psi_v^f\rangle$ is the wave function of the final vibronic state (with energy E_v^f) that results from the excitation via the transition dipole operator $\hat{T}$. The vibronic ground state is expressed as

$$|\Psi_0^i\rangle = |\Phi^0\rangle|0\rangle \tag{11}$$

where $|\Phi^0\rangle$ and $|0\rangle$ represent the electronic and vibrational components of the initial wave function, respectively. Within the harmonic potential ($\mathcal{V}_0$ in eq 5) treatment, the vibrational component ($|0\rangle$) is taken as the direct product of the harmonic oscillator ground states of the relevant vibrational modes.

In the time-independent approach, $P(E)$ is calculated by utilizing the matrix diagonalization method. For this purpose, $|\Psi_v^f\rangle$ is represented in a direct product basis of diabatic electronic state and one-dimensional harmonic oscillator eigenfunctions of the unperturbed Hamiltonian ($\mathcal{T}_N + \mathcal{V}_0$).[27] The resulting Hamiltonian matrix is then diagonalized by using the Lanczos algorithm.[30,31] The eigenvalues yield the exact location of the vibronic energy levels. The relative intensities are then obtained by the squared first components of the Lanczos eigenvectors.[32]

The spectral envelope can also be obtained within the time-dependent approach by Fourier transform of the autocorrelation function,[33]

$$P(E) \propto \int e^{iEt} \langle 0 | \tau^\dagger e^{-i\mathcal{H}t} \tau | 0 \rangle \, dt \tag{12}$$

$$= \int e^{iEt} a_f(t) \, dt \tag{13}$$

τ represents the transition dipole matrix, $\tau^\dagger = (\tau^{S_1}, \tau^{S_{2x}}, \tau^{S_{2y}}, \tau^{S_{3x}}, \tau^{S_{3y}}, \tau^{S_4})$, where $\tau^f = \langle \Phi^f | \hat{T} | \Phi^0 \rangle$. The matrix elements of $\hat{T}$ in the diabatic basis are set to be independent of the nuclear coordinates (generalized Condon approximation) and are taken as unity. The quantity $a_f(t)$ is the time autocorrelation

function, where $a_f(t) = \langle \Psi^f(0) | \Psi^f(t) \rangle$. The initial WP is generated by vertical excitation of the vibrational ground state, $\Psi^f(0) = \tau^f | 0 \rangle$, and its time evolution is given by $|\Psi^f(t)\rangle = e^{-i\mathcal{H}t} |\Psi^f(0)\rangle$. The time-evolved WP may possess components on the vibronically coupled electronic states of CPP; therefore, the composite spectrum is calculated by combining the partial spectra obtained during the WP propagation on each of the six electronic states.[34]

In the present study, the WP propagation calculations are carried out within the multiconfiguration time-dependent Hartree (MCTDH) method, which is designed for quantum dynamical treatment of multidimensional problems.[36] The merits of this method have been demonstrated in numerous studies including absorption, scattering, dissociation, and isomerization processes.[38] The basic MCTDH wave function ansatz is written as

$$\Psi(Q_1, ..., Q_F, t) = \sum_{j_1=1}^{n_1} ... \sum_{j_F=1}^{n_F} A_{j_1 \cdots j_F}(t) \prod_{k=1}^{F} \varphi_{j_k}^{(k)}(Q_k, t) \tag{14}$$

where F represents the number of degrees of freedom (DOFs), and $Q_1, ..., Q_F$ are the nuclear coordinates. The $A_{j_1 \cdots j_F}$ denote the MCTDH expansion coefficients. The basis functions $\varphi_{j_k}^{(k)}$ are the time-dependent single-particle functions (SPFs), and n_k are the number of SPFs used to describe the motion of the kth DOF. The MCTDH equations of motion are solved by representing SPFs in a primitive time-independent basis. A harmonic oscillator discrete variable representation primitive basis is employed in the present study.

Several vibrational DOFs are combined to reduce the dimensionality problem in the MCTDH calculation. The set of DOFs is termed a "particle", and the corresponding MCTDH wave function over p generalized particles is then transformed as

$$\Psi(q_1, ..., q_p, t) = \sum_{j_1=1}^{\tilde{n}_1} ... \sum_{j_p=1}^{\tilde{n}_p} A_{j_1 \cdots j_p}(t) \prod_{k=1}^{p} \varphi_{j_k}^{(k)}(q_k, t) \tag{15}$$

where $q_k = (Q_i, Q_j, ...)$ is the set of DOFs combined together in a single particle and $\tilde{n}_k$ SPFs represent *multimode* SPFs. Note that the technical solution of the MCTDH equations remains unchanged except for replacing the number of DOFs, f, with the number of particles, p.

3.3. Methodological Details. All DFT and TD-DFT calculations in the present study were performed with the Gaussian 09 software package.[35] A complete list of the vibrational modes and the estimated various coupling parameters of CPPs is provided in the Supporting Information. Due to the large number of vibrational modes entering various coupling terms in the vibronic Hamiltonian (eq 5), a full quantum mechanical treatment of the nuclear dynamics of CPPs is impracticable. Thus, here we attempt to perform reduced-dimensional dynamical calculations by considering only the relevant vibrational modes. The selection was based on the coupling strength ($\kappa^2/2\omega^2$ or $\lambda^2/2\omega^2$ or $\lambda'^2/2\omega^2$); therefore, finally we select 26 vibrational modes comprising totally symmetric, JT, and PJT vibrational modes for each CPP. To this end, a set of vibrational modes of $10a_{1g} + 5e_g + 3e_u$ for [6]CPP, $10a_1 + 5e_2 + 3e_1$ for [8]CPP, and $10a_{1g} + 5e_{2g} + 3e_{1u}$ for [10]CPP are considered for the subsequent dynamics simulations.

The WP propagation calculations were carried out with the Heidelberg MCTDH code version 8.4, Revision 8, within the

Table 1. Normal-Mode Combinations and Sizes of the Primitive and Single-Particle Bases Used in the MCTDH Calculations for the Coupled $S_1-S_2-S_3-S_4$ Electronic States of $[n]$CPP

|	normal modes	primitive basis[a]	SPF basis[b] $[S_1, S_{2x}, S_{2y}, S_{3x}, S_{3y}, S_4]$
[6]CPP	$(\nu_5, \nu_{111}, \nu_{145}, \nu_{41x})$	(8, 5, 6, 5)	[6, 5, 5, 6, 6, 6]
	$(\nu_{14}, \nu_{60}, \nu_{106}, \nu_{8y}, \nu_{37x})$	(6, 5, 8, 5, 6)	[5, 5, 5, 6, 6, 5]
	$(\nu_{19}, \nu_{36}, \nu_{67}, \nu_{66}, \nu_{17y})$	(6, 6, 8, 5, 4)	[7, 5, 5, 5, 5, 5]
	$(\nu_{1y}, \nu_{31x}, \nu_{8x}, \nu_{148x})$	(6, 4, 5, 4)	[6, 5, 5, 6, 6, 5]
	$(\nu_{1x}, \nu_{37y}, \nu_{41y}, \nu_{107y})$	(6, 6, 5, 4)	[5, 7, 7, 6, 6, 6]
	$(\nu_{17x}, \nu_{31y}, \nu_{107x}, \nu_{148y})$	(4, 4, 4, 4)	[5, 7, 7, 6, 6, 7]
[8]CPP	$(\nu_{10}, \nu_{162}, \nu_{195}, \nu_{37x})$	(8, 4, 8, 4)	[6, 5, 5, 6, 6, 5]
	$(\nu_{19}, \nu_{82}, \nu_{154}, \nu_{3y}, \nu_{16x})$	(5, 5, 6, 4, 4)	[5, 5, 5, 6, 6, 6]
	$(\nu_{27}, \nu_{50}, \nu_{144}, \nu_{91}, \nu_{7y})$	(5, 4, 6, 5, 6)	[7, 5, 5, 6, 6, 5]
	$(\nu_{1y}, \nu_{13x}, \nu_{3x}, \nu_{198x})$	(6, 4, 4, 4)	[6, 7, 7, 5, 5, 6]
	$(\nu_{1x}, \nu_{16y}, \nu_{37y}, \nu_{23y})$	(6, 4, 4, 4)	[6, 5, 5, 7, 7, 5]
	$(\nu_{7x}, \nu_{13x}, \nu_{23x}, \nu_{198y})$	(6, 4, 4, 4)	[6, 5, 5, 7, 7, 5]
[10]CPP	$(\nu_{14}, \nu_{204}, \nu_{245}, \nu_{54x})$	(8, 5, 6, 5)	[7, 5, 5, 6, 6, 5]
	$(\nu_{21}, \nu_{105}, \nu_{182}, \nu_{8y}, \nu_{26x})$	(6, 5, 8, 5, 5)	[5, 5, 5, 6, 6, 7]
	$(\nu_{35}, \nu_{64}, \nu_{182}, \nu_{115}, \nu_{12y})$	(6, 6, 8, 5, 6)	[7, 5, 5, 6, 6, 5]
	$(\nu_{1y}, \nu_{19x}, \nu_{8x}, \nu_{248x})$	(6, 4, 5, 4)	[6, 7, 7, 5, 5, 6]
	$(\nu_{1x}, \nu_{26y}, \nu_{54y}, \nu_{65y})$	(6, 5, 5, 4)	[6, 5, 5, 7, 7, 5]
	$(\nu_{12x}, \nu_{19y}, \nu_{65x}, \nu_{248y})$	(5, 4, 4, 4)	[5, 6, 6, 7, 7, 5]

[a]The primitive basis for each particle is the product of the one-dimensional bases; e.g., in the case of [6]CPP, the primitive basis for particle 1 (with $\nu_5, \nu_{111}, \nu_{145}, \nu_{41x}$) contains $8 \times 5 \times 6 \times 5 = 1200$ functions, and the full primitive basis consists of a total of 4.403×10^{19} functions. A full primitive basis of 5.01×10^{17} and 6.880×10^{18} functions are utilized to represent the system dynamics in [8]- and [10]CPP, respectively. [b]The SPF basis is the number of single-particle functions used.

multiset formalism.[37] Details of the mode combinations, primitive basis functions, and time-dependent SPFs used in the WP dynamics are listed in Table 1. Six WP calculations (corresponding to S_1, S_{2x}, S_{2y}, S_{3x}, S_{3y}, and S_4 electronic states, where x/y represents the two components of the degenerate state) are carried out by placing the initial WP on each of the six electronic states separately. As stated above, the initial WP is prepared by vertical excitation of the vibrational ground state of the ground electronic state, and the WP is propagated up to 200 fs. The obtained time autocorrelation function is damped with an exponential function of appropriate relaxation time and then Fourier transformed to generate the spectrum.

4. RESULTS AND DISCUSSION

4.1. Vibronic Structure of the S_1 State of [6]CPP. As a first step in our efforts toward understanding the photophysics of the CPPs, we investigate the vibrational energy level structure of the S_1 state of [6]CPP. In Figure 3 we report the theoretical excitation spectrum (indicated by the blue line) computed from the WP dynamics along with the experimental spectrum (indicated by the red line). The time autocorrelation function obtained from the WP calculations is damped with an exponential function of relaxation time 66 fs and then Fourier transformed to generate the spectrum. An appropriate energy shift was applied to the abscissa of the computed spectrum to account for the zero-point vibrational energy. It can be seen from the figure that the overall shape of the experimental spectrum is very well reproduced by the present reduced-dimensionality calculations.

An unambiguous theoretical assignment of the observed low-resolution experimental peaks and corresponding intensities could provide information on the vibronic structure of excited state. Due to the complex and irregular line structure, precise location of the distinct vibronic energy levels cannot be achieved
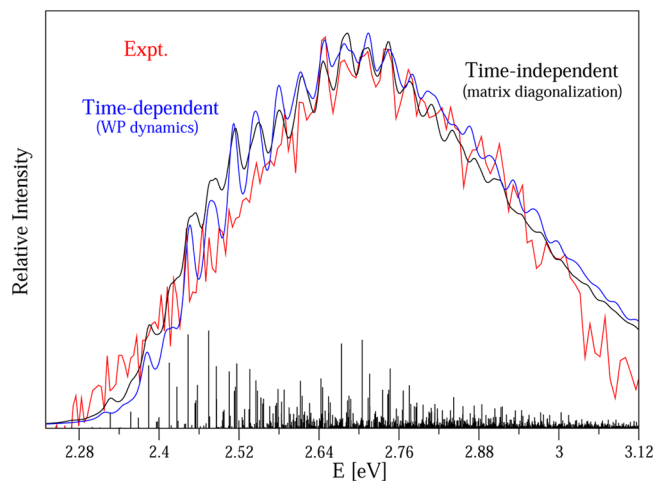
Figure 3. Vibronic spectrum of the S_1 electronic state of [6]CPP. The experimental and the present theoretical results are shown in different colors.

from the present WP dynamics. Therefore, we turn to the alternative approach, namely the time-independent matrix diagonalization method. The vibronic energy level spectrum of the S_1 state calculated by matrix diagonalization is also shown in Figure 3. The stick spectrum (indicated by the black line) is obtained by including 10 relevant a_{1g} vibrational modes (cf. Table 2). A vibrational basis consisting of 10, 5, 5, 4, 2, 2, 2, 4, 2, and 4 harmonic oscillator functions is employed, and the resulting secular matrix with dimension of 2.56×10^5 is then diagonalized using 5000 Lanczos iterations. The convergence is explicitly checked by varying basis functions as well as Lanczos iterations. The stick vibronic lines of Figure 3 are convoluted with a Lorentzian function of 20 meV fwhm, which is equivalent to dampening the time autocorrelation function by a 66 fs

Table 2. Linear Intrastate Coupling Parameters (κ_i) of the S_1 Electronic State of $[n]$CPP Derived from the Electronic Structure Calculations at the TD-B3LYP/6-311G(d) Level of Theory^a

[6]CPP		[8]CPP		[10]CPP	
a_{1g} modes [frequency]	$\kappa^{(S_1)}$	a_1 modes [frequency]	$\kappa^{(S_1)}$	a_{1g} modes [frequency]	$\kappa^{(S_1)}$
ν_5 [0.0101]	−0.0857 (36.0)	ν_{10} [0.0107]	−0.0851 (31.6)	ν_{14} [0.0110]	−0.0770 (24.5)
ν_{14} [0.0270]	−0.0371 (0.94)	ν_{19} [0.0206]	0.0354 (1.48)	ν_{21} [0.0168]	0.0382 (2.59)
ν_{19} [0.0393]	0.0442 (0.63)	ν_{27} [0.0381]	0.0319 (0.35)	ν_{35} [0.0375]	0.0238 (0.20)
ν_{36} [0.0647]	0.0597 (0.42)	ν_{50} [0.0636]	−0.0338 (0.14)	ν_{64} [0.0632]	0.0223 (0.06)
ν_{60} [0.0998]	−0.0318 (0.05)	ν_{82} [0.1002]	0.0219 (0.02)	ν_{104} [0.1005]	0.0181 (0.02)
ν_{66} [0.1005]	0.0155 (0.01)	ν_{90} [0.1019]	0.0059 (0.01)	ν_{105} [0.1021]	0.0318 (0.05)
ν_{67} [0.1023]	−0.0576 (0.16)	ν_{91} [0.1023]	−0.0520 (0.13)	ν_{115} [0.1030]	0.0336 (0.05)
ν_{100} [0.1418]	−0.0226 (0.01)	ν_{138} [0.1423]	0.0151 (0.01)	ν_{174} [0.1422]	0.0104 (0.01)
ν_{106} [0.1514]	−0.1480 (0.48)	ν_{144} [0.1517]	−0.1139 (0.28)	ν_{182} [0.1516]	−0.0943 (0.19)
ν_{111} [0.1580]	−0.0972 (0.19)	ν_{154} [0.1597]	0.0896 (0.16)	ν_{194} [0.1604]	−0.0797 (0.12)
ν_{120} [0.1622]	−0.0357 (0.02)	ν_{162} [0.1613]	−0.0334 (0.02)	ν_{204} [0.1635]	−0.0308 (0.02)
ν_{132} [0.1807]	0.0031 (0.01)	ν_{178} [0.1813]	−0.0025 (0.01)	ν_{224} [0.1814]	0.0014 (0.01)
ν_{145} [0.2003]	−0.2156 (0.58)	ν_{195} [0.2017]	−0.1902 (0.44)	ν_{245} [0.2024]	−0.1698 (0.35)
ν_{161} [0.3938]	−0.0037 (0.01)	ν_{219} [0.3941]	−0.0029 (0.01)	ν_{275} [0.3941]	−0.0025 (0.01)
ν_{174} [0.3963]	0.0075 (0.01)	ν_{234} [0.3959]	−0.0066 (0.01)	ν_{295} [0.3958]	0.0059 (0.01)

^{a}The symmetry, designation, and harmonic frequency (ω_i) of the vibrational modes of the respective CPP in their electronic ground (S_0) state are given. The parameter values and frequencies are given in eV. The numbers in the parentheses represent the dimensionless coupling strengths, $k_i^2/2\omega_i^2$.

envelope, to generate the spectrum. Except for a few minor differences, the time-independent spectrum is also in fairly good agreement with the experiment.

A critical analysis of the theoretical stick spectrum revealed major contributions from five totally symmetric vibrational modes. It is interesting to note that the ν_5 mode is absent in the vibrational progression despite its large excitation strength (cf. Table 2). The energy difference in spacing of the peaks found at ∼0.0298, ∼0.0408, ∼0.10, and ∼0.115 eV can be unambiguously assigned to the excitation of the ν_{14}, ν_{19}, ν_{66}, and ν_{67} modes, respectively. The ν_{14} and ν_{19} modes are deformations of the entire CPP macrocyclic structure, and the latter two modes (ν_{66} and ν_{67}) are C–H out-of-plane bends. An extended progression of the ν_{14} mode, with several overtones (∼0.0591, ∼0.089, and ∼0.1182 eV) and combinations ($\nu_{14} + \nu_{19}$ at ∼0.0706, $\nu_{14} + \nu_{66}$ at ∼0.1297, and $\nu_{14} + \nu_{67}$ at ∼0.1449 eV), is found in the lower energy part of the spectrum. Also, the ν_{145} mode, predominantly C=C stretching, is strongly excited at ∼0.2007 eV, and transition up to its third overtone level is found. The densely packed vibronic levels in the higher energy part of the spectrum hinder further unambiguous assignments; however, with a careful examination, the combinations of ν_{145} with ν_{14}, ν_{19}, ν_{66}, and ν_{67} modes are observed at ∼0.2307, ∼0.2414, ∼0.301, and ∼0.3161 eV, respectively.

As it is evident from the above analysis that the overall spectral features can be well reproduced only with the totally symmetric vibrational modes, it is worthwhile to analyze the topography of the adiabatic PESs along these vibrational modes. The adiabatic PESs of the low-lying excited electronic states of [6]CPP can be obtained by diagonalizing the diabatic electronic Hamiltonian introduced in eq 5 as

$$\mathbf{S}^\dagger(\mathcal{H} - \mathcal{J}_N \mathbf{1})\mathbf{S} = V \tag{16}$$

where $\mathbf{S}$ is an orthogonal adiabatic-to-diabatic transformation matrix.[27] In Figure 4, we show the one-dimensional cuts of the multidimensional PESs of the low-lying excited states along the dimensionless normal coordinate of the ν_{145}, keeping the others fixed at their equilibrium value $Q = 0$. The computed vertical excitation energies added with the harmonic ground-state
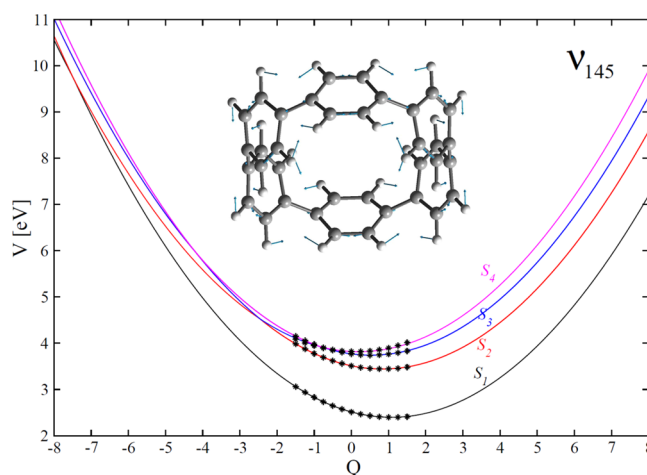
Figure 4. Adiabatic potential energies of the S_1, S_2, S_3, and S_4 electronic states of [6]CPP along the dimensionless normal coordinates of a totally symmetric vibrational mode (ν_{145}). The equilibrium geometry of [6]CPP in its electronic ground state ($1A_{1g}$) corresponds to $Q = 0$.

potential are shown by the points in the diagram. It can be seen that the computed ab initio energies are well represented by the linear vibronic coupling (LVC) model.

The S_1–S_2 (and S_1–S_3) VC via e_u symmetry vibrational modes is rather weak (cf. Table 3 and Supporting Information, Table SI8) and does not contribute in the S_1 absorption band. This is clearly seen from the simulated spectra shown in Figure 3. The spectral features are (nearly) identical in both the time-dependent and time-independent spectra. Note that the former spectrum is generated by including 10 a_{1g} plus 3 e_u vibrational modes and the latter by only 10 a_{1g} vibrational modes. However, the weak VC associated with the S_1–S_2 curve crossing (cf. Figure 4) is sufficient for symmetry breaking of the S_1 state, thereby partially allowing the dipole-forbidden $S_0 \rightarrow S_1$ transition. As a result, this transition is seen in the absorption spectrum with very low intensity. With increasing CPP size, the S_1–S_2 vertical energy gap decreases (cf. Figure 5) and the vibronic mixing becomes stronger. A convincing confirmation can be seen in the increase

Table 3. Linear Interstate Coupling Parameters (λ_i') for the S_1−S_2 Excited Electronic States of the $[n]$CPP Derived from Electronic Structure Calculations at the TD-B3LYP/6-311G(d) Level of Theory[a]

[6]CPP		[8]CPP		[10]CPP	
e_u modes [frequency]	$\lambda'_{(S1-S2)}$	e_1 modes [frequency]	$\lambda'_{(S1-S2)}$	e_{1u} modes [frequency]	$\lambda'_{(S1-S2)}$
ν_{17} [0.0360]	0.0044 (0.01)	ν_{23} [0.0281]	0.0161 (0.10)	ν_{12} [0.0104]	0.0239 (2.64)
		ν_{51} [0.0670]	0.0087 (0.01)	ν_{23} [0.0195]	0.0018 (0.01)
		ν_{80} [0.0995]	0.0125 (0.01)	ν_{26} [0.0230]	0.0105 (0.10)
		ν_{215} [0.3934]	0.0169 (0.01)	ν_{65} [0.0659]	0.0174 (0.03)
		ν_{232} [0.3959]	0.0149 (0.01)	ν_{102} [0.1001]	0.0083 (0.01)
				ν_{116} [0.1031]	0.0051 (0.01)
				ν_{147} [0.1263]	0.0060 (0.01)
				ν_{183} [0.1516]	0.0362 (0.03)
				ν_{192} [0.1602]	0.0202 (0.01)
				ν_{246} [0.2028]	0.0598 (0.04)

[a]The symmetry, designation, and harmonic frequency (ω_i) of the vibrational modes of the respective CPP in their ground electronic (S_0) state are given. The parameter values and frequencies are given in eV. The numbers in parentheses represent the dimensionless coupling strengths, $\lambda_i'^2/2\omega_i^2$.
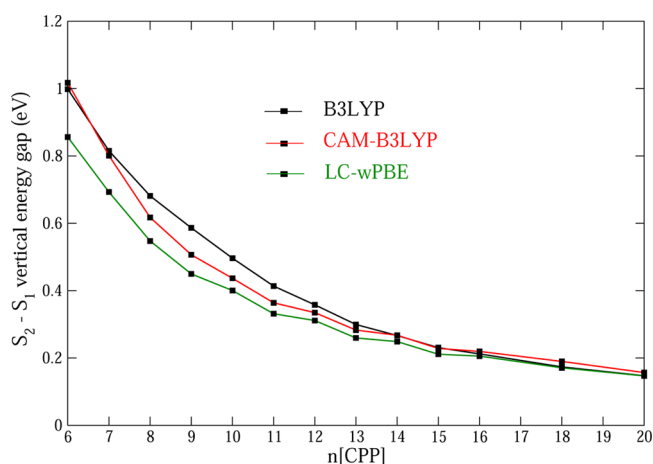
Figure 5. Energy gap between the S_1 and S_2 electronic states of $[n]$CPPs estimated with different functionals at the TD-DFT level of theory using the 6-311G(d) basis set.

of not only the number of vibrational modes with nonzero interstate coupling constant but also the corresponding coupling strength (cf. Table 3). On the basis of these observations, one can conclude that the dipole-forbidden $S_0 \rightarrow S_1$ transition is "increasingly allowed" with increasing CPP size, and this is reflected in the observed experimental transition dipole moments[15] and S_1 band intensity pattern.[4,7,8,12−14,16,17,19,20]

4.2. Structural Distortions in the S_1 State of CPPs. Figure 6a depicts the theoretical absorption spectra of the S_1 state of $[n]$CPPs ($n = 6, 8,$ and 10) calculated from WP dynamics. Details of the relevant vibrational modes and the primitive as well as SPFs are collected in Table 1. As stated above, a damping of 66 fs is applied to the autocorrelation function to generate the respective spectral envelope. The $S_0 \rightarrow S_1$ vertical excitation energy of CPPs tends to increase with increasing ring size (cf. Figure 6b), subsequently resulting in the observed blue-shift of the excitation peaks as reported in recent nonlinear excitation measurements.[13]

The CPPs reveal relatively similar S_1 band shape with well-structured vibronic progression; however, a characteristic variation of intensity with molecular size is observed. On closer scrutiny of the intensity profiles, one might notice a specific feature: the energetic location of the highest intensity peak. The highest intensity peak tends to shift toward the lower energy part of the spectrum with increasing ring size. More precisely, $[6]$CPP
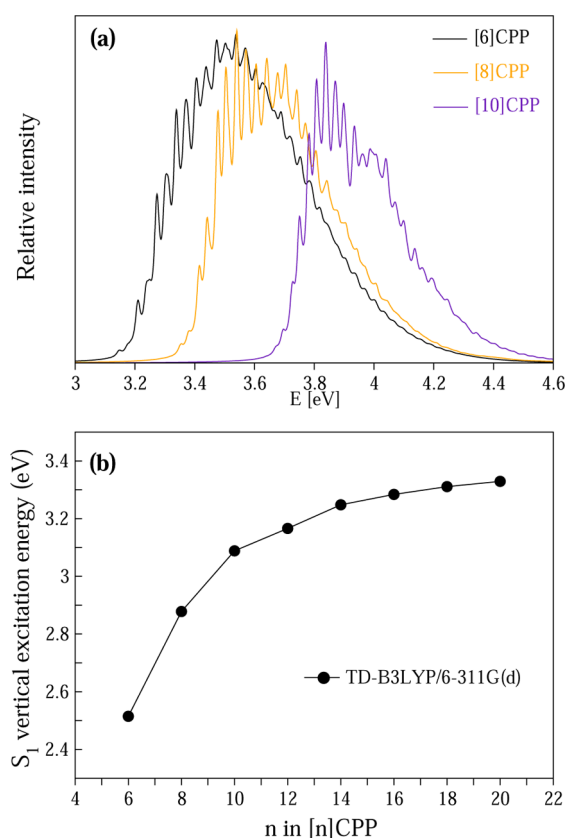
Figure 6. (a) S_1-state vibronic spectra of CPPs calculated from the time-dependent wave packet calculations. (b) $S_0 \rightarrow S_1$ vertical excitation energy of CPPs. See the text for details.

has the highest intensity at the center of the spectrum. On the other hand, the highest intensity peak can be seen closer to the 0−0 peak instead of the center of the spectrum for $[10]$CPP. As is seen from the above spectral analysis of $[6]$CPP, the totally symmetric vibrational modes alone can reproduce the experimental spectrum; hence, we examine the trends in the vibrational frequencies and corresponding κ for interpretation of the intensity pattern. Surprisingly, the frequency of a particular relevant vibrational mode remains more or less similar irrespective of ring size, but the corresponding κ_i decreases with increasing ring size. For example, consider the 13th row of Table 2. The vibrational modes ν_{145} of $[6]$CPP, ν_{195} of $[8]$CPP,

Table 4. Estimated Vertical Excitation Energy (VEE), Emission Energy, and Stabilization Energy (E_s) of the S_1 State of $[n]$CPP within the TD-B3LYP/6-31G(d) Level of Theory[a]

		emission		E_s		maximum change		
	VEE	TD-B3LYP/6-31G(d)	expt[b]	TD-B3LYP/6-31G(d)	LVC	bond length (Å)	bond angle	dihedral angle[c]
[6]CPP	2.52	1.29	–	0.66	0.69	0.5	3.9	30.9
[8]CPP	2.86	1.89	2.33	0.49	0.57	0.3	2.4	21.9
[10]CPP	3.05	2.28	2.64	0.39	0.46	0.2	1.6	15.0

[a]All the parameters are in eV. The maximum changes in the bond length (Å), bond angle, and dihedral angle of the optimized structures of the S_0 and S_1 states are given. All angles are in degrees. The estimated E_s from the LVC model is also given for comparison. [b]The experimental values (λ_{max}) are taken from ref 19. [c]The dihedral angle represents the torsional angle between two paraphenylene planes.

and ν_{245} of [10]CPP have frequencies of 0.2003, 0.2017, and 0.2024 eV, respectively. But the corresponding κ_i values are −0.2156, −0.1902, and −0.1698 eV. As described in section 4.1, the κ_i values represent the slope of the adiabatic potential function with respect to the dimensionless normal coordinate of the vibrational mode i, and thus reflect the topography of the S_1 PES within the Franck−Condon region. This implies that the higher the gradient magnitude, the steeper the adiabatic PESs. From Table 2, it can be concluded that [6]CPP has the steepest S_1 PES, and the steepness decreases with increasing ring size. These findings are consistent with the picosecond domain structural relaxation trend observed from the fluorescence up-conversion experiment.[19]

To illustrate the extent of structural distortions, we refer to Figure 4. $Q = 0$ represents the equilibrium geometry of the S_0 state. Upon photoexcitation to the S_1 state, a shift in the equilibrium geometry occurs along with the distortion of the dimensionless coordinates of the ν_{145} mode, and thus a new minimum develops on the S_1 state around $Q = +1.0$. The stabilization energy, E_s, caused by such a shift of the equilibrium geometry in the multimode effect can be estimated as

$$E_s = \sum_i \frac{\kappa_i^2}{2\omega_i} \tag{17}$$

Those values are collected in Table 4 for each CPP studied here. Alternatively, it is possible to estimate E_s from electronic structure calculations, where it is defined as the energy difference between the vertical excitation at the ground-state equilibrium geometry and the global minimum of the S_1 state. The values estimated at the TD-B3LYP/6-31G(d) level of theory are also given in Table 4. It is gratifying to see that the present model Hamiltonian quite accurately reproduces the electronic structure calculation estimates. The relatively large E_s value (∼0.7 eV) of [6]CPP indicates that the associated structural changes seem to be larger compared to the other CPPs, consistent with our previous MD study.[26]

Internal coordinates describe the extent of structural changes of a molecule better than normal coordinates. For this purpose, we compare the internal coordinates of the optimized S_0 and S_1 geometries obtained from DFT and TD-DFT calculations, respectively. Due to the large number of internal coordinates of CPP, comparison of each individual coordinate is quite tedious. Therefore, only the maximum variation in the bond length, bond angle, and dihedral angle is considered and collected in Table 4. The estimates are consistent with the previous theoretical studies.[19] We observe that the major distortion upon photo-excitation is the variation of the dihedral angle, i.e., the angle between two adjacent phenyl units. The variation in the coordinates directly relates to E_s: the larger the variation, the larger the energy stabilization.

4.3. Fluorescence Stokes Shift. The $S_1 \rightarrow S_0$ emission energies of CPPs obtained at the TD-B3LYP/6-31G(d) level of theory are provided in Table 4 along with the experimental data. The trend of increasing excitation and emission energy with increasing ring size is fully consistent with experimental results.[13,19] The most important feature is the observed large Stokes shift in [6]CPP. According to Table 4, the S_1 state of [6]CPP is subjected to large structural distortions corresponding to the estimated $E_s \approx 0.7$ eV, leading to the observed large Stokes shift. As a consequence, the emission energy falls into the near-infrared (near-IR) range of the electromagnetic spectrum. This explains the absence of detectable visible fluorescence in the experiment.[4] In principle, the near-IR emission of [6]CPP should be observable, but with only very low quantum yield due to weak VC.

The increase in excitation energy and decrease of E_s with increasing ring size give rise to the observed "blue-shifted" fluorescence in smaller CPPs. Although the blue-shift phenomenon is apparent from the table, the theoretical calculations for emission from S_1 underestimate the experimental emission λ_{max}^{em}. One plausible explanation for this discrepancy is that the calculated absolute energy may not correspond directly to the λ_{max}^{em} of the CPP. Hence, we compare the difference between the two CPPs. The λ_{max}^{em} values of [8]- and [10]CPPs are 533 nm (2.33 eV) and 470 nm (2.64 eV), respectively, and the difference is 0.31 eV.[19] The theoretical value of 0.39 eV is in accord with the experiment.

The larger CPPs, above [14]CPP, reveal somewhat similar excitation energies (∼3.3 eV, cf. Figure 6b) with a negligible E_s contribution (due to very minor geometrical changes upon photoexcitation) and tend to emit at relatively constant energy. Here we should emphasize that the emission from S_2 (in addition to the S_1 state) in larger CPPs is most likely expected as the S_1 and S_2 states become nearly degenerate (cf. Figure 5).

The vertical excitation and emission energies calculated with the TD-CAM-B3LYP/def-SV(P) level of theory[26] were slightly overestimated compared to the TD-B3LYP/6-31G(d) calculations. The complete set of data is provided in the Supporting Information (Table SI9).

4.4. Fluorescence Lifetimes and Quantum Yields. Next, we theoretically investigate the ring-size-dependent fluorescence properties reported from different experimental groups. We begin with one of the fundamental fluorescence properties, the radiative decay rate (k_r). For convenience, we refer to the fluorescence data reported by Fujitsuka et al.[19] The experimental k_r values as a function of the number of paraphenylene units n are plotted in Figure 7. Assuming that the spontaneous emission process essentially occurs from $S_1 \rightarrow S_0$, then the expression for k_r is written as[39,40]
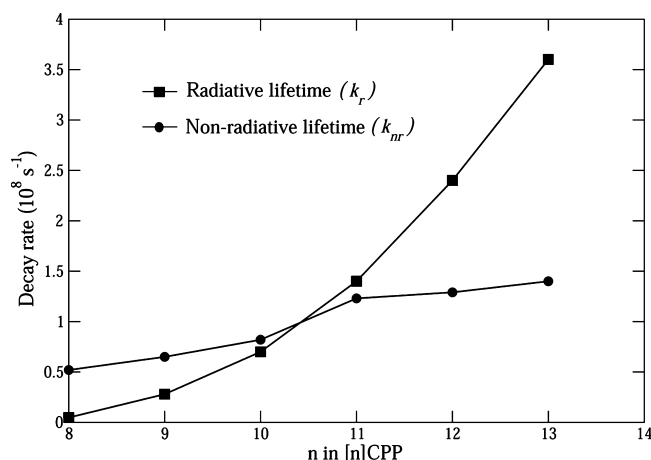
Figure 7. Experimental radiative and nonradiative decay rates (10^8 s^{-1}) of CPPs taken from ref 19.

$$k_r = \frac{4}{3}\frac{\Delta E^3}{c^3}\mu_{10}^2 \qquad (18)$$

where ΔE denotes the $S_1 \rightarrow S_0$ emission energy, c is the speed of light, and μ_{10}^2 represents the transition dipole strength in atomic units. μ^2 commonly describes the measure of "allowedness" of the transition and is governed primarily by the symmetry selection rule. To a first approximation, the $S_1 \rightarrow S_0$ emission is dipole-forbidden, i.e., $\mu_{10}^2 = 0$, as the S_0 and S_1 states of CPP possess even parity (cf. Figure 2). However, the $S_1–S_2$ vibronic mixing, as described in section 4.1, leads to a nonzero μ_{10}^2. With this, now it is clear that k_r depends solely on ΔE: the ΔE (both theoretical and experimental) value increases with increasing ring size and thus reflects the observed experimental k_r trend.[19]

Let us quantify the μ_{10}^2, or the degree of allowedness, of the $S_1 \rightarrow S_0$ emission of CPPs on the basis of eq 18. Upon substituting the experimental k_r (taken from ref 19) and calculated ΔE (from Table 4) values of [8]- and [10]CPP in eq 18, one can derive the μ_{10}^2 ratio relationship:

$$\frac{[10]\text{CPP}}{[8]\text{CPP}} \approx 8.3 \qquad (19)$$

This implies that the degree of allowedness of the $S_1 \rightarrow S_0$ transition in [10]CPP is ~8 times higher than in [8]CPP. This is exemplified by the evaluated $S_1–S_2$ interstate VC parameters shown in Table 3. With this description, the monotonically increasing k_r shown in Figure 7 is unambiguously attributed to ΔE and μ_{10}^2, where both quantities tend to increase with increasing ring size.

The other important fluorescence property, the quantum yield Φ_{fl}, deserves more attention here. The experimental reported Φ_{fl} values of [8]- and [10]CPP are 0.084 and 0.46, respectively, and the efficiency tends to increase with increasing CPP size.[19] The Φ_{fl} in general is defined in terms of k_r:

$$\Phi_{fl} = \frac{k_r}{k_r + k_{nr}} \qquad (20)$$

where k_{nr} represents the overall nonradiative decay rate. Here, k_{nr} is taken as the sum of the internal conversion (IC) and the intersystem crossing (ISC) rates, i.e., $k_{nr}^{IC} + k_{nr}^{ISC}$, and the possible nonradiative process due to photochemical reaction is ignored. With the help of both known experimental quantities, Φ_{fl} and k_r, and using eq 20, k_{nr} is estimated for each CPP. The obtained data

are plotted in Figure 7. Surprisingly, nonradiative processes are dominant in smaller CPPs. It is interesting to note that, although the k_{nr} values have the same order of magnitude, a noticeable increase with increasing ring size is seen.

As $k_{nr} = k_{nr}^{IC} + k_{nr}^{ISC}$, one has to consider the contribution of both the IC and ISC processes for a meaningful interpretation of the observed k_{nr}. The roles of singlet–triplet mixing and associated ISC decay dynamics seem to be important, not only in molecular systems but also in carbon nanotube photoluminescence;[41,42] however, such an investigation is out of the scope of the present study. Instead, here we provide a qualitative description of the intramolecular deactivation by IC processes. As the crossings of adiabatic potentials of the low-lying electronic states of CPP are evident from Figure 4, the energetic location of the global minimum of the S_1 state with respect to the seam minimum of the $S_1–S_2$ and $S_1–S_3$ conical intersections (CIs) plays a crucial role in the radiationless deactivation process. From the LVC model estimates provided in Table 5, we observe that the energy

Table 5. Relative Energies of [n]CPP[a]

	[6]CPP	[8]CPP	[10]CPP
S_1 VEE	2.51	2.88	3.09
S_1 min.	1.82	2.31	2.63
$S_1–S_2$ CI min.	5.70	4.30	4.30
$S_1–S_3$ CI min.	5.90	4.65	4.53

[a]The vertical excitation energy (VEE) of the S_1 state is calculated at the TD-B3LYP/6-311G(d) level. The minimum of the S_1 state and the minima of $S_1–S_2$ and $S_1–S_3$ conical intersections (CIs) are estimated within the LVC model. All quantities are given in eV.

separation between S_1 and CI minima, although large, tends to decrease with increasing ring size. Following the relative energetic trends in the table, IC processes are expected to strongly influence the fluorescence decay dynamics of larger CPPs.

4.5. λ_{max} of the Absorption Spectrum. One of the other interesting features of the photoexcited CPPs is the constant absorption λ_{max} irrespective of ring size.[12,19] The origin of this feature is discussed here. The theoretical spectrum associated with the $S_2–S_3–S_4$ electronic manifold of CPP is displayed in the left-side panels of Figure 8. In the lower traces of the panels, the partial spectra corresponding to the individual electronic states of CPP are plotted in different colors. A Lorentzian line width fwhm = 20 meV is applied to reveal vibronic structure in the spectral envelopes. In addition, a low-resolution composite spectrum (indicated by a black line) in the upper traces is also shown in each panel. The composite spectrum of the CPP is the weighted combination of the partial spectra of resolution of fwhm = 220 meV. An appropriate shift is applied to the abscissa of each panel to reproduce the experimental λ_{max}. The overall shape of the experimental spectrum of [6]CPP (indicated by the green line in the top panel) is fairly well reproduced. The shoulder peak observed in the longer wavelength part of the experimenatal spectrum is attributed to the S_2 state. It is clearly seen that the overlapping S_3 and S_4 bands contribute to the λ_{max}. The scenario is different in [8]- and [10]CPP, where the overlapping S_2 and S_3 vibronic bands produce the highest intensity in the spectrum. In [8]CPP, the vibronic band corresponding to the S_4 state is seen at shorter wavelengths. Due to the partial overlap with the S_2 and S_3 bands, the S_4 band appears close to the λ_{max} in [10]CPP.

The observed vibronic band overlapping pattern of CPPs is better understood from the corresponding adiabatic PESs
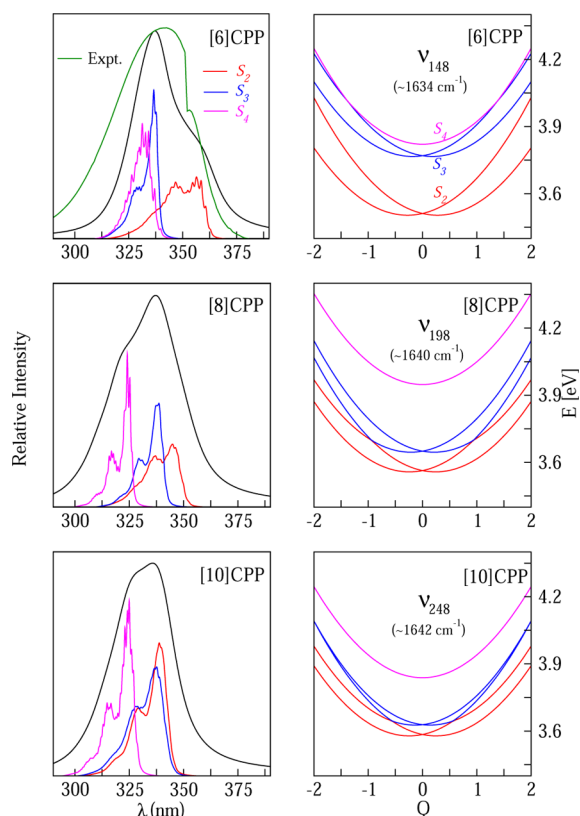
Figure 8. (Left panels) S_2–S_3–S_4 vibronic spectra of CPP. The partial spectra (shown in different colors) of CPP are obtained from the WP calculations, and a resolution of 20 meV is applied for each partial spectrum. The composite spectrum (black line) of CPP, with a resolution of 220 meV, is generated by combining the partial spectra with equal weighting. The experimental spectrum of [6]CPP is also shown in the upper panel (green line). (Right panels) Adiabatic potential energies of the S_2, S_3, and S_4 electronic states of CPP along the dimensionless normal coordinates of the degenerate vibrational mode. See the text for details.

displayed in the right-side panels of Figure 8. The adiabatic potential energies obtained by diagonalizing the vibronic Hamiltonian (eq 5) are plotted against the dimensionless normal coordinate of the one of the degenerate vibrational modes of CPP. The vibrational mode is of predominantly a C=C stretching motion, and the corresponding frequency is also provided in the panel for each CPP. As stated in the Introduction, the S_2 and S_3 states are doubly degenerate and undergo JT splitting as shown in these panels. In the case of [6]CPP (cf. top panels), the S_2 state is relatively well separated from the energetically close-lying S_3 and S_4 states and appears as a shoulder peak in the spectrum. It should be understood that the mixing of vibronic levels of the latter states is the main source for the observed λ_{max}. On the other hand, the S_2 and S_3 states are closer in [8]CPP, and even closer in [10]CPP, subsequently leading to the observed band overlapping pattern (cf. lower panels).

Note that the interstate coupling among the S_2, S_3, and S_4 electronic states of CPP is not included in the present nuclear dynamics. As these states undergo strong mixing, one would expect that the inclusion of interstate coupling in the Hamiltonian could result in severe perturbation of the underlying vibronic structure. A detailed investigation of the impact of S_2–S_3–S_4 interstate coupling in the absorption spectrum of CPP is planned for a future study.

Finally, the computations performed in the present work refer to gas-phase processes. For an accurate comparison of the experimental optical properties of CPPs, one must include the solvent effects.

5. SUMMARY AND CONCLUDING REMARKS

A detailed quantum chemical and quantum dynamics description of the experimental UV/vis photophysical property trends of [n]CPPs has been presented. The structural and dynamical aspects of the low-lying singlet excited electronic states of the [6]-, [8]-, and [10]CPPs were critically examined to interpret the absorption and emission properties. A model diabatic Hamiltonian within the linear vibronic coupling approach was constructed considering the vibronic coupling among the low-lying excited electronic states and 26 relevant vibrational degrees of freedom to elucidate the absorption spectrum of CPP. The coupling parameters of the Hamiltonian were determined by employing DFT/TD-DFT methods. Quantum nuclear dynamics studies on the interacting electronic states have been performed to investigate the underlying vibronic structure of the spectrum. Through subsequent analysis in conjunction with excited-state optimized structures, the fluorescence properties have been characterized. The key findings are as follows:

(i) The formally dipole-forbidden transition between the S_0 and S_1 states is increasingly allowed with increasing ring size owing to the VC of the S_1 state with higher excited states through non-totally symmetric vibrational modes.

(ii) With increasing ring size, the S_1–S_2 vertical energy gap decreases and VC effects become dominant. The increased S_1 band intensity in the experimental absorption spectrum with increasing ring size is one such effect. This feature is difficult to observe in experimental UV/vis spectra due to the strong absorption caused by excitation to the higher-lying states.

(iii) The large overlap of the close-lying S_2, S_3, and S_4 vibronic bands is responsible for the observed intense broad band. The overlapping pattern of the underlying vibronic bands results in a constant absorption maximum wavelength λ_{max}, regardless of the ring size.

(iv) A blue-shift of the fluorescence with increasing ring size was found in the theoretical calculations, consistent with the experiment. The formally dark S_1 state increasingly "borrows" fluorescence quantum yield via non-adiabatic coupling to bright higher-lying states as the ring size increases.

(v) The structural changes upon photoexcitation tend to decrease with increasing ring size. [6]CPP is subjected to large structural changes, accounting for the large Stokes shift. According to quantum chemical calculations, [6]CPP exhibits a near-IR fluorescence with emission at ~960 nm. This explains the absence of detectable "visible fluorescence" in the experiment.

(vi) The larger CPPs (above [14]CPP) possess somewhat similar $S_1 \leftarrow S_0$ excitation energies (~3.3 eV) and undergo very minor geometrical changes upon photoexcitation. As a consequence, they tend to exhibit a relatively constant $S_1 \rightarrow S_0$ emission energy.

Our present findings could provide important new insights into the excited-state dynamics of CPPs. Most importantly, we find that the large density of states close to S_1 dramatically alters the photophysics in these large, highly symmetric macromolecules. Elucidation of underlying mechanisms of radiative

and nonradiative processes within the description of electron–vibration (vibronic) interactions has direct analogy with and offers useful perspective in understanding and interpreting the electron–phonon interactions and their effects on the optical and electronic properties of similar such systems, which should be useful for understanding such properties also in the case of low-dimensional carbon nanotubes.[43–47]

■ ASSOCIATED CONTENT

Ⓢ Supporting Information

Harmonic vibrational frequencies of the S_0 state, VC parameters, and Cartesian coordinates of the S_1 optimized structures. This material is available free of charge via the Internet at http://pubs.acs.org.

■ AUTHOR INFORMATION

Corresponding Authors
*E-mail: sivaranjana.reddy@e.mbox.nagoya-u.ac.jp.
*E-mail: sirle@chem.nagoya-u.ac.jp.

Notes
The authors declare no competing financial interest.

■ ACKNOWLEDGMENTS

■ REFERENCES

(1) Jasti, R.; Bhattacharjee, J.; Neaton, J. B.; Bertozzi, C. R. *J. Am. Chem. Soc.* **2008**, *130*, 17646–17647.

(2) Jasti, R.; Bertozzi, C. R. *Chem. Phys. Lett.* **2010**, *494*, 1–7.

(3) Sisto, T. J.; Golder, M. R.; Hirst, E. S.; Jasti, R. *J. Am. Chem. Soc.* **2011**, *133*, 15800–15802.

(4) Xia, J.; Jasti, R. *Angew. Chem., Int. Ed.* **2012**, *51*, 2474–2476.

(5) Xia, J.; Bacon, J. W.; Jasti, R. *Chem. Sci.* **2012**, *3*, 3018–3021.

(6) Darzi, E. R.; Sisto, T. J.; Jasti, R. *J. Org. Chem.* **2012**, *77*, 6624–6628.

(7) Evans, P. J.; Darzi, E. R.; Jasti, R. *Nat. Chem.* **2014**, *6*, 404–408.

(8) Li, P.; Sisto, T. J.; Darzi, E. R.; Jasti, R. *Org. Lett.* **2014**, *16*, 182–185.

(9) Takaba, H.; Omachi, H.; Yamamoto, Y.; Bouffard, J.; Itami, K. *Angew. Chem., Int. Ed.* **2009**, *48*, 6112–6116.

(10) Omachi, H.; Matsuura, S.; Segawa, Y.; Itami, K. *Angew. Chem., Int. Ed.* **2010**, *49*, 10202–10205.

(11) Segawa, Y.; Miyamoto, S.; Omachi, H.; Matsuura, S.; Senel, P.; Sasamori, T.; Tokitoh, N.; Itami, K. *Angew. Chem., Int. Ed.* **2011**, *50*, 3244–3248.

(12) Segawa, Y.; Fukazawa, A.; Matsuura, S.; Omachi, H.; Yamaguchi, S.; Irle, S.; Itami, K. *Org. Biomol. Chem.* **2012**, *10*, 5979–5984.

(13) Nishihara, T.; Segawa, Y.; Itami, K.; Kanemitsu, Y. *J. Phys. Chem. Lett.* **2012**, *3*, 3125–3128.

(14) Sibbel, F.; Matsui, K.; Segawa, Y.; Studera, A.; Itami, K. *Chem. Commun.* **2014**, *50*, 954–956.

(15) Nishihara, T.; Segawa, Y.; Itami, K.; Kanemitsu, Y. *Chem. Sci.* **2014**, *5*, 2293–2296.

(16) Yamago, S.; Watanabe, Y.; Iwamoto, T. *Angew. Chem., Int. Ed.* **2010**, *49*, 757–759.

(17) Iwamoto, T.; Watanabe, Y.; Sakamoto, Y.; Suzuki, T.; Yamago, S. *J. Am. Chem. Soc.* **2011**, *133*, 8354–8361.

(18) Iwamoto, T.; Watanabe, Y.; Sadahiro, T.; Haino, T.; Yamago, S. *Angew. Chem., Int. Ed.* **2011**, *50*, 8342.

(19) Fujitsuka, M.; Cho, D. W.; Iwamoto, T.; Yamago, S.; Majima, T. *Phys. Chem. Chem. Phys.* **2012**, *14*, 14585–14588.

(20) Kayahara, E.; Patel, V. K.; Yamago, S. *J. Am. Chem. Soc.* **2014**, *136*, 2284–2287.

(21) Wong, B. M. *J. Phys. Chem. C* **2009**, *113*, 21921–21927.

(22) Sundholm, D.; Tauberta, S.; Pichierri, F. *Phys. Chem. Chem. Phys.* **2010**, *12*, 2751–2757.

(23) Segawa, Y.; Omachi, H.; Itami, K. *Org. Lett.* **2010**, *12*, 2262–2265.

(24) Wong, B. M.; Lee, J. W. *J. Phys. Chem. Lett.* **2011**, *2*, 2702–2706.

(25) Segawa, Y.; Fukazawa, A.; Matsuura, S.; Omachi, H.; Yamaguchi, S.; Irle, S.; Itami, K. *Org. Biomol. Chem.* **2012**, *10*, 5979–5984.

(26) Camacho, C.; Niehaus, T. A.; Itami, K.; Irle, S. *Chem. Sci.* **2013**, *4*, 187–195.

(27) Köppel, H.; Domcke, W.; Cederbaum, L. S. *Adv. Chem. Phys.* **1984**, *57*, 59–246.

(28) (a) Lichten, W. *Phys. Rev.* **1967**, *164*, 131–142. (b) Smith, F. T. *Phys. Rev.* **1969**, *179*, 111–123. (c) O'Malley, T. F. *Adv. At. Mol. Phys.* **1971**, *7*, 223–249. (d) Pacher, T.; Cederbaum, L. S.; Köppel, H. *Adv. Chem. Phys.* **1993**, *84*, 293–391.

(29) Wilson, E. B.; Decius, J. C.; Cross, P. C. *Molecular vibrations*; McGraw-Hill: New York, 1955.

(30) Lanczos, C. *J. Res. Nat. Bur. Stand.* **1950**, *45*, 255–282.

(31) Cullum, J.; Willoughby, R. *Lanczos Algorithms for Large Symmetric Eigenvalue Problems*; Birkhäuser: Boston, 1985; Vols. I and II.

(32) Köppel, H.; Domcke, W. In *Encyclopedia of Computational Chemistry*; Schleyer, P. v. R., Ed.; Wiley: Chichester, 1998; pp 3166–3182.

(33) Köppel, H.; Döscher, M.; Baldea, I.; Meyer, H.-D.; Szalay, P. G. *J. Chem. Phys.* **2002**, *117*, 2657–2671.

(34) Domcke, W.; Köppel, H.; Cederbaum, L. S. *Mol. Phys.* **1981**, *43*, 851–875.

(35) Frisch, M. J.; Trucks, G. W.; Schlegel, H. B.; Scuseria, G. E.; Robb, M. A.; Cheeseman, J. R.; Scalmani, G.; Barone, V.; Mennucci, B.; Petersson, G. A.; Nakatsuji, H.; Caricato, M.; Li, X.; Hratchian, H. P.; Izmaylov, A. F.; Bloino, J.; Zheng, G.; Sonnenberg, J. L.; Hada, M.; Ehara, M.; Toyota, K.; Fukuda, R.; Hasegawa, J.; Ishida, M.; Nakajima, T.; Honda, Y.; Kitao, O.; Nakai, H.; Vreven, T.; Montgomery, J. A., Jr.; Peralta, J. E.; Ogliaro, F.; Bearpark, M.; Heyd, J. J.; Brothers, E.; Kudin, K. N.; Staroverov, V. N.; Kobayashi, R.; Normand, J.; Raghavachari, K.; Rendell, A.; Burant, J. C.; Iyengar, S. S.; Tomasi, J.; Cossi, M.; Rega, N.; Millam, N. J.; Klene, M.; Knox, J. E.; Cross, J. B.; Bakken, V.; Adamo, C.; Jaramillo, J.; Gomperts, R.; Stratmann, R. E.; Yazyev, O.; Austin, A. J.; Cammi, R.; Pomelli, C.; Ochterski, J. W.; Martin, R. L.; Morokuma, K.; Zakrzewski, V. G.; Voth, G. A.; Salvador, P.; Dannenberg, J. J.; Dapprich, S.; Daniels, A. D.; Farkas, Ö.; Foresman, J. B.; Ortiz, J. V.; Cioslowski, J.; Fox, D. J. *Gaussian 09*, Revision C.01; Gaussian, Inc.: Wallingford, CT, 2010.

(36) (a) Meyer, H.-D.; Manthe, U.; Cederbaum, L. S. *Chem. Phys. Lett.* **1990**, *165*, 73–78. (b) Manthe, U.; Meyer, H.-D.; Cederbaum, L. S. *J. Chem. Phys.* **1992**, *97*, 3199–3213. (c) Beck, M. H.; Jäckle, A.; Worth, G. A.; Meyer, H.-D. *Phys. Rep.* **2000**, *324*, 1–105.

(37) Worth, G. A.; Beck, M. H.; Jäckle, A.; Meyer, H.-D. *The MCTDH Package*, Version 8.2; University of Heidelberg: Heidelberg, Germany, 2000; Meyer, H.-D., Version 8.3, 2002; Version 8.4, 2007. See http://mctdh.uni-hd.de.

(38) Manthe, U.; Meyer, H.-D.; Cederbaum, L. S. *J. Chem. Phys.* **1992**, *97*, 3199–3213. (b) Meyer, H.-D. *Wiley Interdiscip. Rev.: Comput. Mol. Sci.* **2012**, *2*, 351–374. (c) Meyer, H.-D.; Quéré, F. L.; Léonard, C.; Gatti, F. *J. Chem. Phys.* **2006**, *329*, 179–192.

(39) Lounis, B.; Orrit, M. *Rep. Prog. Phys.* **2005**, *68*, 1129–1179.

(40) Nienhuis, G.; Alkemade, C. T. J. *Physica B+C* **1976**, *81*, 181–188.

(41) Dresselhaus, M. S.; Dresselhaus, G.; Saito, R.; Jorio, A. *Annu. Rev. Phys. Chem.* **2007**, *58*, 719–747.

(42) Tretiak, S. *Nano Lett.* **2007**, *7*, 2201–2206.

(43) Goupalov, S. V.; Satishkumar, B. C.; Doorn, S. K. *Phys. Rev. B* **2006**, *73*, No. 115401(1–6).

(44) Yin, Y.; Vamivakas, A. N.; Walsh, A. G.; Cronin, S. B.; Unlu, M. S.; Goldberg, B. B.; Swan, A. K. *Phys. Rev. Lett.* **2007**, *98*, No. 037404(1–4).

(45) Shreve, A. P.; Haroz, E. H.; Bachilo, S. M.; Weisman, R. B.; Tretiak, S.; Kilina, S.; Doorn, S. K. *Phys. Rev. Lett.* **2007**, *98*, No. 037405(1–4).

(46) Luer, L.; Gadermaier, C.; Crochet, J.; Hertel, T.; Brida, D.; Lanzani, G. *Phys. Rev. Lett.* **2009**, *102*, No. 127401(1−4).

(47) Pisana, S.; Lazzeri, M.; Casiraghi, C.; Novoselov, K. S.; Geim, A. K.; Ferrari, A. C.; Mauri, F. *Nat. Mater.* **2007**, *6*, 198−201.